Materials & Design 258 (2025) 114598

Contents lists available at ScienceDirect

Materials & Design

journal homepage: www.elsevier.com/locate/matdes

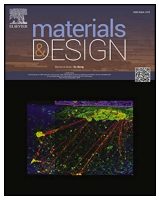

Understanding and detection of process instabilities in wire arc directed energy deposition additive manufacturing using meltpool imaging and machine learning☆

André Ramalho [a,b,*], Anis Assad [b,c], Benjamin Bevans [b,d], Fernando Deschamps [e], Telmo G. Santos [a,f], J.P. Oliveira [g,**], Prahalada Rao [b]

[a] UNIDEMI, Department of Mechanical and Industrial Engineering, NOVA School of Science and Technology, Universidade NOVA de Lisboa, Caparica 2829-516, Portugal
[b] Grado Department of Industrial and Systems Engineering, Virginia Tech, Blacksburg, VA, USA
[c] University of Southern Denmark, Department of Technology and Innovation, Sønderborg, Denmark
[d] Sooner Advanced Manufacturing Laboratory, University of Oklahoma, Norman, OK, USA
[e] Pontifícia Universidade Católica do Paraná, Imaculada Conceição 1155, 80215-901 Curitiba, Brazil
[f] Laboratório Associado de Sistemas Inteligentes, LASI, 4800-058 Guimarães, Portugal
[g] CENIMAT/I3N, Department of Materials Science, NOVA School of Science and Technology, Universidade NOVA de Lisboa, Caparica 2829-516, Portugal

ARTICLE INFO

Keywords:
Wire arc directed energy deposition
Wire arc additive manufacturing (WAAM)
Porosity
Humping
Meltpool imaging
Process-aware machine learning

ABSTRACT

This work concerns the wire arc directed energy deposition (WA-DED) additive manufacturing process. The objectives were two-fold: (1) observe and understand, through in-operando high-speed meltpool imaging, the causal dynamics of two common WA-DED process instabilities, namely, humping and humping-induced porosity; and (2) leverage the high-speed meltpool imaging data within machine learning algorithms for real-time detection of process instabilities. Humping and humping-induced porosity are leading stochastic causes of poor WA-DED part quality that occur despite extensive optimization of processing conditions. It is therefore essential to understand, detect and control the causal meltpool phenomena linked to these instabilities. Accordingly, we used a high-speed camera to capture the meltpool dynamics of multi-layer depositions of ER90S-G steel parts and meltpool flow behavior related to process instabilities were demarcated and quantified. Next, physically intuitive meltpool morphology signatures were extracted from the imaging data. These signatures were used in a machine learning model trained to autonomously detect process instabilities. This novel process-aware machine learning approach classified onset of instabilities with ~85 % accuracy (F1-score), outperforming black-box deep learning models (F1-score <66 %). These results pave the way for a physically intuitive process-aware machine learning strategy for monitoring and control of the WA-DED process.

1. Introduction

The objective of this work was two-fold: (1) observe and understand, through in-operando high-speed imaging, the link between *wire arc directed energy deposition* (WA-DED) meltpool dynamics and two common stochastic process instabilities, namely, humping and humping-induced porosity that occur despite extensive optimization of processing parameters; and (2) leverage the high-speed meltpool imaging data for in-situ monitoring and detection of process instabilities.

The directed energy deposition (DED) family of additive manufacturing (AM) processes use focused energy in the form of electric arc, plasma, laser, or an electron beam to melt and deposit material layer-by-layer [1]. The material can either take the form of powder or wire. The deposition of material in three dimensions is accomplished via

☆ This article is part of a special issue entitled: 'Additive Manufacturing' published in Materials & Design.

* Corresponding author at: UNIDEMI, Department of Mechanical and Industrial Engineering, NOVA School of Science and Technology, Universidade NOVA de Lisboa, Caparica 2829-516, Portugal.
** Corresponding author at: CENIMAT/I3N, Department of Materials Science, NOVA School of Science and Technology, Universidade NOVA de Lisboa, Caparica 2829-516, Portugal.
E-mail addresses: afg.ramalho@campus.fct.unl.pt (A. Ramalho), jp.oliveira@fct.unl.pt (J.P. Oliveira).

https://doi.org/10.1016/j.matdes.2025.114598
Received 18 February 2025; Received in revised form 30 July 2025; Accepted 14 August 2025
Available online 17 August 2025

the relative motion of the part and energy source, typically with a gantry-driven axis or a robotic arm.

The WA-DED process, depicted in Fig. 1, resembles arc-based welding, such as metal inert gas (GMAW) and tungsten inert gas welding (GTAW) [2]. Hence, the process is also known as wire arc additive manufacturing (WAAM) [3]. In WA-DED, a metallic wire is used as feedstock material. Typical materials include alloys of iron, titanium, and aluminum [4]. An electric potential is applied between the tip of the electrode and surface of the previously deposited layer. This potential difference ionizes a stream of shielding gas, and generates a plasma column, which in turn creates an electric arc. Current flows through the electrically conductive plasma, and provides the heat necessary to melt the tip of the feedstock wire. The heat from the plasma also melts the material in the previously deposited layer, generating a pool of molten material, called the meltpool (or weld pool), into which the wire material is fed. The molten droplet, formed at the wire tip, and meltpool are protected by the shielding gas. The shielding gas prevents oxidation of the meltpool, stabilizes the electric arc, and influences the mode of material transfer [5]. Contamination from the atmosphere and surrounding debris in the meltpool are particularly detrimental to weld quality as they are liable to create porosity [6]. Contingent on the material and application, the shielding gas can be inert, e.g., argon or helium, or active, e.g., carbon dioxide, hydrogen and mixtures of the foregoing with inert gases. The combination of shielding gas type and flow rates influences the quality of the deposited layer.

The relatively large magnitude of energy supplied by the electric arc in WA-DED, relative to laser-based DED, enables high material deposition rates [7]. The WA-DED process is capable of deposition rates approaching 10 kg per hour, viz., almost five times that of laser powder (LP-DED) and laser-wire (LW-DED) processes [7–10]. Further, WA-DED is considerably economical compared to LP-DED given the low cost and availability of welding wire in contrast to metal powder. The high deposition rates afforded by WA-DED are valuable for rapid manufacturing of large volume parts. For example, Nycz and co-workers [11] from the Oakridge National Laboratory used a robot-based WA-DED setup to manufacture a functional excavator attachment with an approximate weight of 180 kg in about 5 days of continuous printing at deposition rates approaching 7 kg per hour. Recently, additive friction stir deposition (AFSD), which is a highly energy and material efficient, non-fusion based AM process, has emerged as an alternative to WA-DED for manufacturing large parts [12].

Amongst the drawbacks, compared to LW-DED and LP-DED, the geometric resolution, accuracy, and repeatability of WA-DED is relatively poor, and substantial post-process machining is often required [13,14]. The relatively high energy input necessary to achieve larger volumetric deposition rates, coupled with stochasticity inherent to the WA-DED process, engenders complex thermo-physical interactions linked to flaw formation, such as porosity, humping, lack-of-fusion, cold and hot cracking [2,15].

In this work, we aim to understand and detect two common WA-DED process instabilities induced by stochastic variations in the meltpool dynamics, these are: (i) *humping,* and (ii) humping with surface porosity, termed *humping-induced porosity*. These process instabilities, exemplified in Fig. 2, occur despite extensive *a priori* optimization of processing parameters. We leverage the in-operando high-speed meltpool imaging data with machine learning algorithms to monitor the process and consequently detect the onset of humping and humping-induced porosity [16,17].

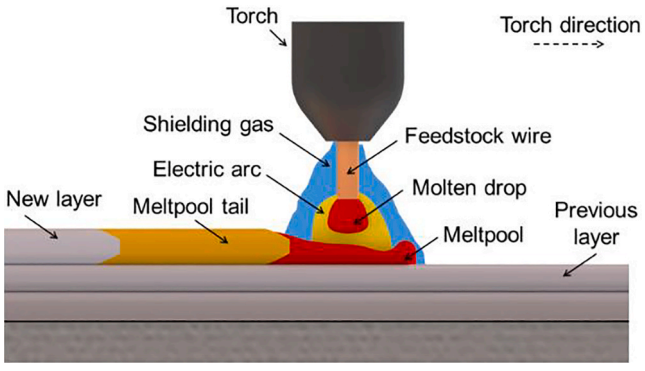

Fig. 1. Process schematic of wire arc directed energy deposition (WA-DED).

Shown in Fig. 2 are images of three as-processed thin-wall parts, and their corresponding cross-section under nominal (stable), humping, and humping-induced porosity conditions. In the nominal thin-wall sample, Fig. 2(a), no macroscopic flaws were evident in the cross-section. The sample in Fig. 2(b) displayed a periodic undulation of the layer, termed *humping.* The part affected by *humping-induced porosity,* as demarcated in the cross-section image in Fig. 2(c), shows porosity in the interior of the part in addition to poor surface quality. The foregoing instabilities result from complex meltpool-process interactions encompassing electromagnetic forces, heat flux, fluid-flow, solidification phenomena, and stochastically-driven aspects associated with high-speed welding [18–20]. The meltpool dynamics at the root of these phenomena will be further elucidated in Sec. 4 with the aid of high-speed optical imaging.

The distinction between nominal, humping and humping-induced porosity conditions during WA-DED is important to monitor and detect. Despite extensive parameter optimization, the WA-DED process is afflicted by inherent stochastic effects, such as disruption of gas flow, variation in machine kinematics, vibration, contamination of the feedstock material, amongst others, which are known to disrupt the stability of the meltpool [21]. Further, with the advent of hybrid additive-subtractive WA-DED machines, a layer afflicted by humping flaws may be machined and re-deposited [13]. However, the deeply embedded internal pores in humping-induced porosity would require

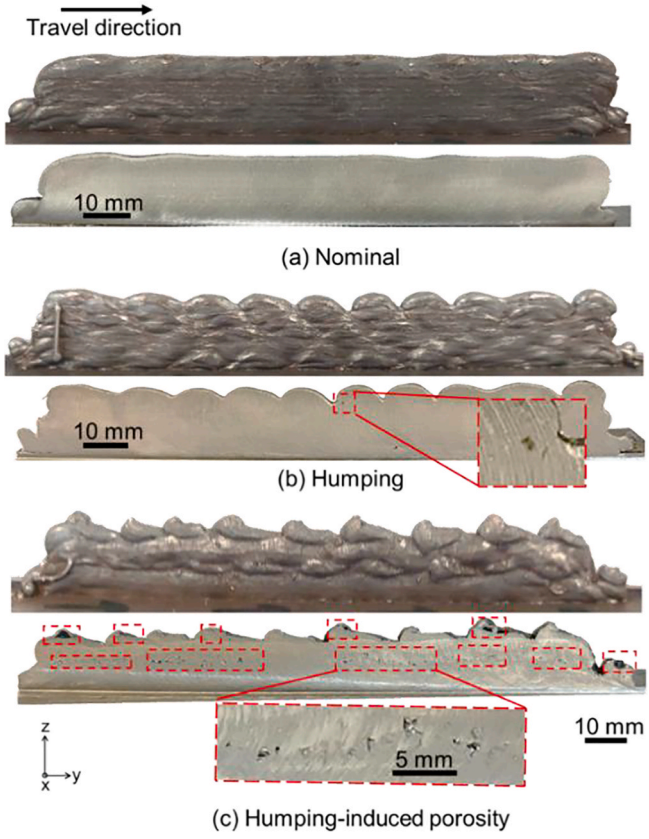

Fig. 2. WA-DED thin-wall samples produced for this work, representative of the three different part conditions investigated in this work: (a) Nominal, (b) Humping and (c) Humping-induced porosity.

machining of several layers to remove with hybrid WA-DED.

The origin of humping-induced porosity is illustrated in Fig. 3, where a representation of internal porosity from X-ray CT is displayed for two samples derived from original data acquired in this study. As shown in Fig. 3(a), the layer height variations due to humping-induced undulations in the previous layer causes fluctuations in the distance between the welding nozzle and top of the previous layer. Consequently, the contact tip-to-work distance (CTWD), varies incessantly and stochastically during humping along the direction of deposition. The increase in the CTWD in valley regions curtails the flow of the shielding gas and compromises effective protection of the meltpool. Left unchecked, this condition is exacerbated, resulting in humping-induced porosity. For example, Fig. 3(b) illustrates a sample and its corresponding X-ray CT cross-section with minor degrees of humping, where the expected CTWD variation during the deposition was low. No internal porosity was observed in the X-ray CT for this sample. However, the sample in Fig. 3(c) was affected by severe humping, resulting in internal porosity, characteristic of humping-induced porosity.

In this context, researchers have demonstrated that stochastic-induced disruptions or alterations of the shielding gas flow can cause porosity in arc-based processes [22]. Insufficient flow of the shielding gas can be caused by clogging of the nozzle due to spatter or increase in CTWD [22]. The shielding gas protects the freshly formed molten droplet at the tip of the wire and the meltpool against contamination by foreign debris and oxidation [15]. As recently demonstrated by Bevans *et al.* [21], disruption of the shielding gas enables particulate debris and oxygen to enter the reactive meltpool, which in turn causes poor material consolidation and porosity. Likewise, Bitharas *et al.* [23] reported elevated oxygen concentration on the surface of the meltpool induced by low gas flow rates, resulted in porosity in GMAW-fabricated deposits of DH36 high strength structural steel.

Fig. 4 underscores the transient and complex stochastic dynamics inherent to humping instability. Shown in Fig. 4 is a region of a 9-layer tall thin wall fabricated with previously optimized processing parameters. This deposition demonstrates both flaw-free layers at the macroscopic scale, and layers exhibiting localized defects. In Fig. 4(a), during the course of deposition of layer 4, the onset of onset of localized humping instability is discerned with a characteristic valley-like region. However, as shown in Fig. 4(b), the instability self-corrects during deposition of layer 5. As evident from Fig. 4(c), the process continues unimpeded by humping, resulting in the deposition of nominal, flaw-free layers up to layer 8. However, in layer 9, represented in Fig. 4(d), the humping instability re-manifests.

The novelty of this work is in identifying and predicting the onset of humping and humping-induced porosity in WA-DED through in-operando high-speed imaging of the meltpool. To the best of our knowledge, this is one of the first works that experimentally observes and elucidates the causal meltpool dynamics that are symptomatic of the foregoing process instabilities for a multi-layer WA-DED part. Further, we also estimated the variation of meltpool flow velocities at the nominal, humping, and humping-induced porosity process regimes. As will be summarized in the forthcoming literature review in Sec. 2, while humping and humping-induced porosity has been explained with the aid of theoretical simulations of the meltpool, largely for single track depositions, experimental observation of the meltpool dynamics concerning these instabilities for multi-layer constructs has remained elusive.

The approach implemented for predicting the onset of process instabilities is summarized in Fig. 5. We manufactured multi-layer thin-wall WA-DED mild steel parts under different processing conditions. During deposition of the thin-wall parts, the meltpool dynamics were captured using a high-speed imaging camera *as illustrated in* Fig. 5*(a). Image processing is applied to the acquired WA-DED images,* Fig. 5*(b), to identify the contour of the meltpool region. From this contour,* four physically intuitive meltpool morphology features (process signatures) were extracted from the high-speed images *as represented in* Fig. 5*(c). Finally, as presented in* Fig. 5*(d),* these meltpool process signatures are used as inputs to computationally tractable and interpretation amenable machine learning models, such as shallow artificial neural networks, logistic regression, and k-nearest neighbors. These models were trained (supervised learning) to classify the WA-DED process state into the following three categories: nominal, humping, and humping-induced porosity.

Since the approach uses physically intuitive process signatures obtained from the meltpool images, it is termed *process-aware machine learning*. The approach is benchmarked against a black-box deep machine learning model, that, instead of extracting process signatures, uses the meltpool images directly for detecting the state of the process. The computational complexity of the deep learning models compared to the tractability of the process-aware machine learning approach, is detrimental to model deployment for real-time monitoring and transferability.

The rest of this paper is organized as follows. Summarized in Sec. 2 is the current literature in WA-DED process monitoring. Described in Sec. 3 is the WA-DED setup and the design of experiments. Sec. 4 details the correlation of the meltpool dynamics and estimation of meltpool velocity under nominal, humping, and humping-induced porosity process states. Sec. 5 discusses the meltpool morphology features extracted from the high-speed imaging data, and their use in a process-aware machine learning model for detection of instabilities. Finally, conclusions and avenues for future work are summarized in Sec. 6.

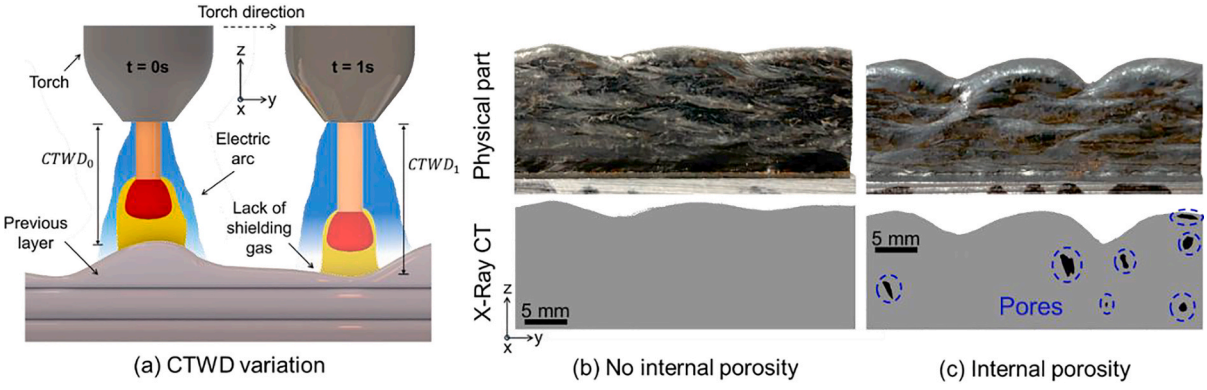

Fig. 3. (a) Changes in CTWD when the previously deposited layer exhibits a humping flaw. (b) X-ray CT of a humping flawed sample with no internal porosity. (c) X-ray CT of a sample with humping flaw, with internal porosity (humping-induced porosity). The increase in distance from CTWD0 to CTWD1 induces a lack of shielding gas protection to the meltpool. The CTWD distance illustrated only considers the previously deposited layer and not the deposited material of the present layer.

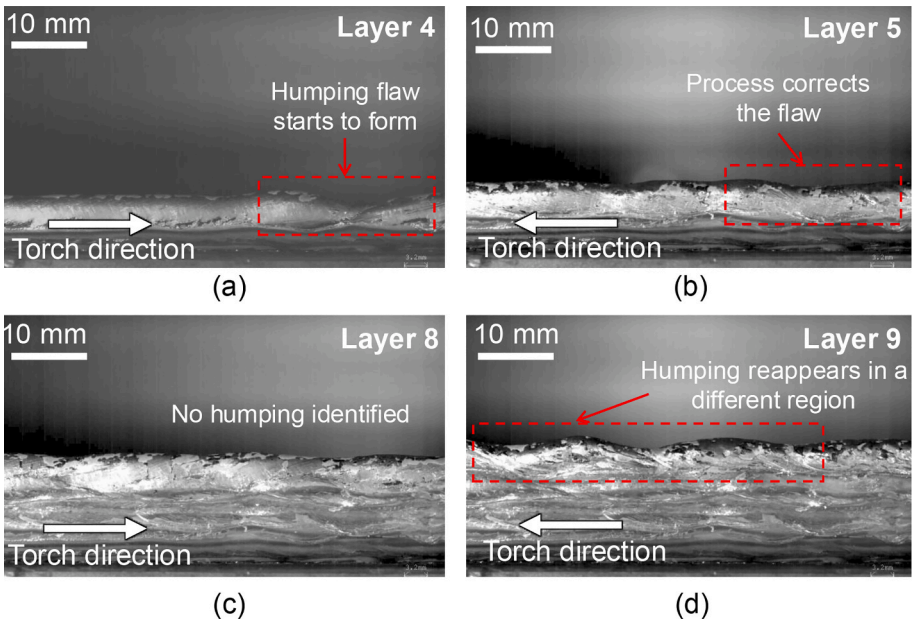

Fig. 4. Occurrence of humping instability in WA-DED is stochastic and transient. (a) Humping flaw formed in the right side of the deposited layer 4. (b) The process self-corrects and humping instability is not evident during deposition of layer 5. (c) Humping is not observed even during deposition of layer 8. (d) Humping appears again on layer 9, on a different region from where it was originally identified.

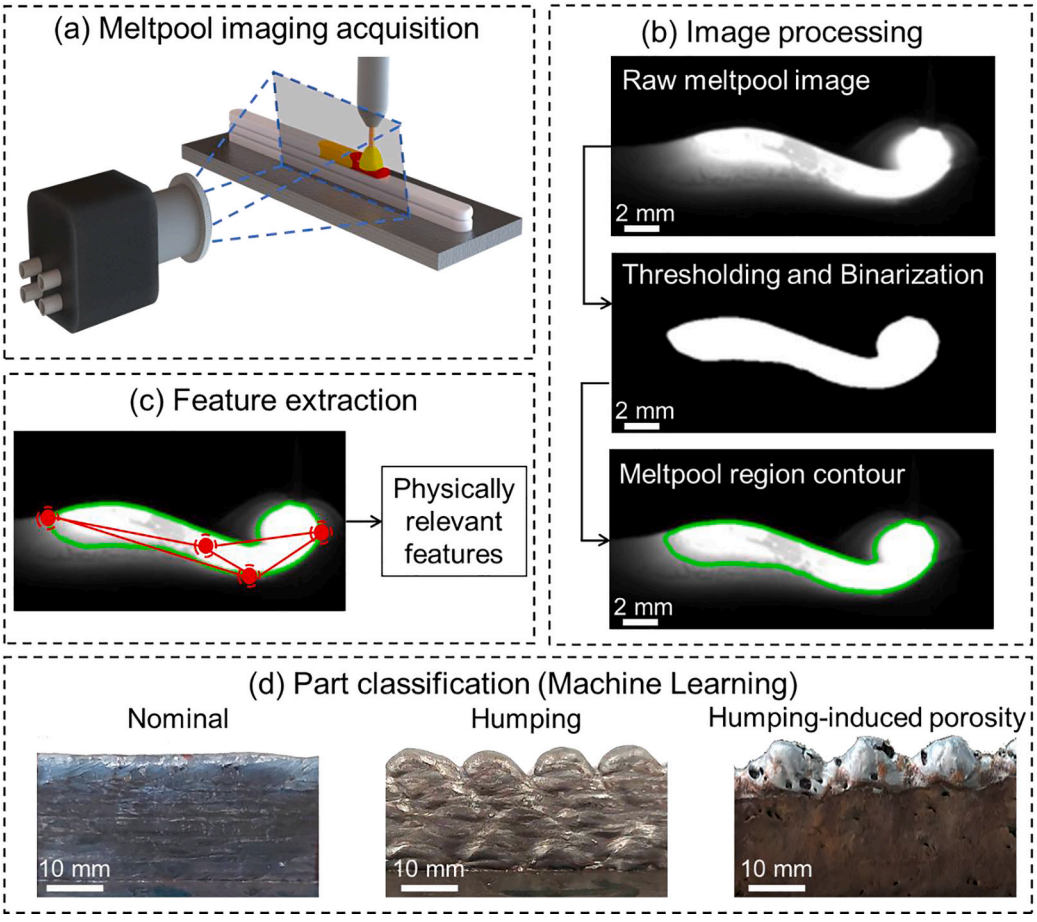

Fig. 5. Overview of the proposed approach. (a) Raw meltpool images are captured by the high-speed camera. (b) Image processing through binarization and thresholding is used to identify the meltpool region contour. (c) The identified meltpool region contour is used to extract meltpool morphology features (process signatures). (d) These process signatures are employed for classifying the WA-DED process state into nominal, humping, or humping-induced porosity.

2. Prior work in detecting humping and humping-induced porosity

The humping phenomena has been studied in the context of flaw formation in high-speed welding [24,25]. Nguyen *et al.* [26] studied the occurrence of humping in gas metal arc welding (GMAW) using meltpool imaging with a CCD camera. They varied welding positions and the nature of shielding gases. It was found that use of active shielding gas at higher welding speeds mitigated humping. The authors concluded that using active shielding gas, compared to inert shielding gasses, increased the width of the meltpool, which in turn increased the lateral flow of molten material during deposition. This effect facilitates the flow of material to the front of the meltpool, thus suppressing humping.

Cho *et al.* [27] used both numerical simulation and meltpool imaging acquired by a high-speed camera to explain the meltpool-level dynamics symptomatic of humping in GMAW depositions of ASTM A-36 steel. First, the arc pressure and momentum, causes the meltpool to flow in the opposite direction of the torch. The backward flow results in material aggregation toward the tail of the meltpool. Consequently, the material depleted front region of the meltpool solidifies rapidly forming a valley, whilst the material accumulated at the tail solidifies slower to form a hump. The observations in this work are consistent with the findings of Cho *et al.* [27] and will be further elucidated in Sec. 4.

To suppress humping in GMAW, researchers have proposed multi-wire deposition. Wu *et al.* [28], introduced a twin-wire approach where two electrodes, one trailing the other, are employed. Each wire creates a separate electric arc with its own meltpool. The distance between the two wires is adjusted such that their respective meltpools can merge during deposition. Employing two trailing wires creates a so-called push–pull effect where the pressure of the trailing arc counteracts the high backward momentum of the meltpool deposited by the leading wire. This suppresses the aggregation of material in the tail of the meltpool, and mitigates humping flaw. By relying on the same physical principle of the push–pull effect, Gu *et al.* [29] proposed a triple wire approach to suppress humping.

Adebayo *et al.* [30] studied the occurrence of humping flaws in WA-DED through the production of ER70S-6 steel thin-walls with varying torch travel speed and wire feed speed. They demonstrated a threshold value for these parameters beyond which the humping phenomena originates. Albeit, the parameter thresholds are contingent on the characteristics of the feedstock material, processing parameters and machine. We note that in practice, humping and humping-induced porosity often occur despite extensive parameter optimization on account of the inherent stochasticity of the process [30]. For example, researchers have observed that minor variations in the ambient temperature and environmental conditions, gas flow rates, presence of contaminants in the wire, among others, are liable to cause process instabilities [31,32]. Hence, stochastic factors can have a significant influence on humping related phenomena.

Table 1 summarizes representative literature in vision-based monitoring and control of the WA-DED process. Li et al. [33] used a CMOS camera to acquire images of the solidified top layer. This layer image was subsequently used with a deep learning model for the classification of three types of defects: superficial (surface) porosity, grooves, and slag inclusions. Likewise, Xia et al. [34] used a commercially available welding camera to acquire WA-DED meltpool images. These images were used as inputs to a convolutional neural network trained to identify different process states, including humping and superficial porosity, achieving model accuracies of ~97 %. However, a majority of the existing process monitoring forays in WA-DED employ purely data-driven black-box machine learning-based models and do not provide insights into the causal process physical phenomena. The novelty of this work is that it uses fundamental insights from the process dynamics to extract physically intuitive meltpool morphology features. These features are subsequently used for detection of humping and humping-induced porosity flaws.

Table 1
Summary of the literature using vision-based sensing for monitoring the status of the WA-DED processes.

Author	Aim	Sensor
Haussler *et al.* [35]	Monitor behavior of arc at varying torch angles	High-speed camera
Zhan *et al.* [36]	Detection of wire deflection	Commercial welding camera
Reisgen *et al.* [37]	Torch height control	Imaging sensor (unspecified)
Franke *et al.* [38]	Control CTWD and spatter using semantic segmentation and connected component analysis	Commercial welding camera
Xiong *et al.* [39]	Layer height control with a PID controller	CCD camera
Xiong *et al.* [40]	Layer width control with a fuzzy controller	CCD camera
Li *et al.* [33]	Layer flaw detection with a black-box convolutional neural network (CNN).	CMOS camera
Xia *et al.* [34]	Layer flaw detection with a CNN.	Commercial welding camera

3. Experiments

The open architecture WA-DED setup used in this work is shown in Fig. 6. The setup integrates a custom-built welding torch and three-axis gantry motion system. A Lincoln Electric CITOWAVE III 520 welding machine and a DMU W500 wire feeder were connected to the torch. Parts were produced using ER90S-G mild steel feedstock wire with a diameter of 1 mm. A stationary high-speed imaging camera (FASTCAM Mini WX50 with a Schneider Emerald 4.0/80 lens) was placed perpendicular to the axis of motion of the torch. To limit the saturation of the imaging sensor, on account of the broadband high magnitude electromagnetic radiation emitted by the WA-DED process, an 800 nm long pass optical filter was placed between the camera and the torch.

The high-speed camera acquired images at a rate of 1000 frames per second with a resolution of 1280 × 800 pixels. The shutter speed was set to 10^{-4} s, with f/16 aperture. Dynamic voltage and current readings were also acquired at a sampling rate of 10 kHz. Voltage was measured between the welding torch and the part substrate; a Hall Effect sensor was used for measurement of current. The voltage and hall effect sensor data were ineffective for detection of process states and are hence not reported in this work.

Fig. 6(a) also details the positioning of the camera relative to the process. The lens of the camera was placed 400 mm away from the torch which enabled the acquisition of images within a horizontal field of view of 50 mm *as illustrated in* Fig. 6*(b)*. The camera was manually focused on the tip of the feedstock wire when it was positioned at the center of the camera's field of view. Images were acquired in the central 50 mm of the sample, to negate the effect of start-and-stop process instabilities at the beginning and end of a layer. No external illumination was used to avoid the visualization of elements external to the meltpool.

Fig. 7 shows a sample frame acquired by the high-speed camera. In each frame, three regions can be identified: meltpool, electric arc, and solidified layer. While the meltpool and the electric arc, highlighted in Fig. 7, emit the most electromagnetic energy in the operating optical range, the solidified layer around the meltpool is also visible. The area encompassing the meltpool and the arc will be further analyzed for understanding the meltpool dynamics. Since the arc and meltpool have similar pixel intensities, it is difficult, if not impossible, to discern a separation boundary between the two. Henceforth, the arc and the meltpool area shall be referred to as the meltpool region.

Thin-wall parts with a single pass per layer were deposited using a zig-zag deposition strategy, as illustrated in Fig. 8(a), with the resulting thin-wall part depicted in Fig. 8*(b)*. All the samples, ER90S-G mild steel, were deposited on carbon steel substrates using a mixture of Argon + CO_2 as shielding gas, with a volume ratio of 92:8, respectively, and a flow rate of 20 L•min^{-1}. The layer length was maintained at 150 mm;

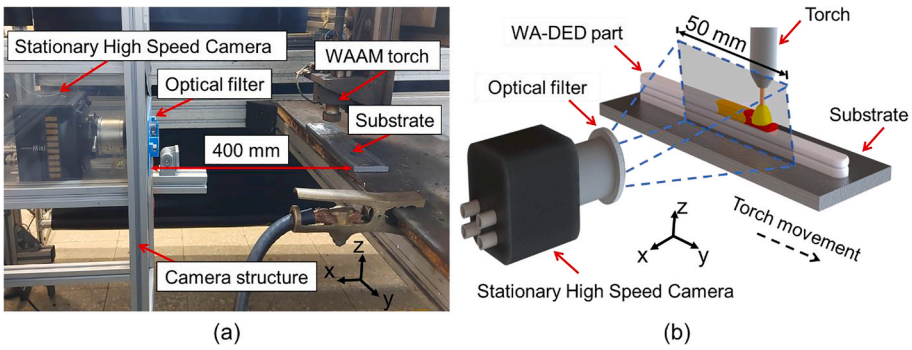

Fig. 6. Sensor setup for WA-DED meltpool image acquisition. (a) Relative placement of the stationary high-speed camera. (b) Field-of-view of the high-speed camera, spanning 50 mm in the y-axis.

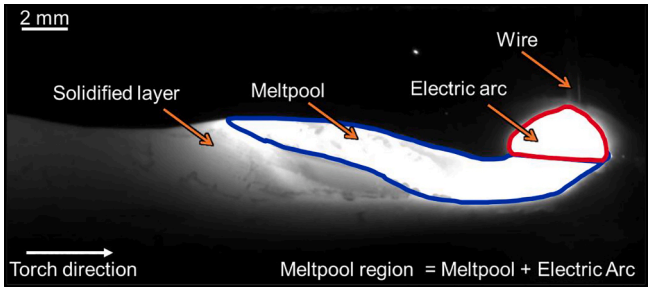

Fig. 7. Identification of regions captured by the high-speed camera. The meltpool and the electric arc form the meltpool region, which is analyzed in this work.

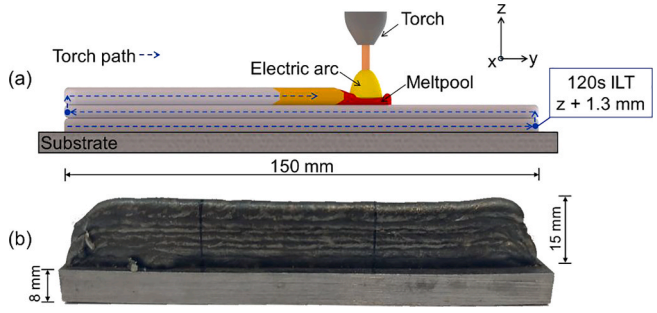

Fig. 8. (a) CAD model of WA-DED thin-wall with torch path. (b) Example of a Nominal labeled part, produced using the defined torch path.

CTWD was fixed at 8 mm; and interlayer time (ILT) or inter-pass time was 120 s.

In this work, the process operates in short circuit transfer mode, wherein the transfer of material from the wire to the meltpool occurs through physical contact. The molten tip of the wire is in contact with the meltpool, before detaching from the wire. As summarized in Fig. 9, two processing parameters were varied, namely, the travel speed of the torch (v, [mm.min^{-1}]), and welding power (P, [W]). Consequently, the heat input, Q, varies as a function of P and v as follows: $Q = \frac{P}{v}[J/mm]$. The variations in Q as a function of v and P are known to influence the meltpool behavior, and effect the nature of the deposited bead [41]. Based on extensive *a priori* experiments the processing parameter combinations reported in Fig. 9 manifest in nominal, humping, and humping-induced porosity in the samples.

These experiments were conducted in a lab environment where environmental factors, such as ambient temperature and pressure, humidity, gas flow rate, etc., were tightly controlled. However, as evident previously in the context of Fig. 4 and current literature (Sec. 2),

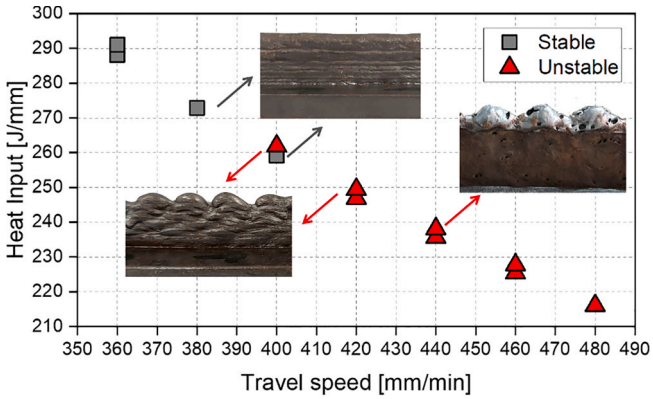

Fig. 9. Process parameters used for sample production. As travel speed increases and heat input decreases the deposition process becomes unstable, however a region of overlap where both flaw free and humping flawed parts were obtained can be identified.

humping-related instability is inherently transient and stochastic in nature. Therefore, under practical conditions a minor stochastic variation in any of the ambient factors could cause humping or humping-induced porosity.

The aim of the experimental design was to understand and detect process instabilities in WA-DED. Accordingly, *a total of 12* sample parts were produced to achieve the three process conditions, nominal, humping, and humping-induced porosity, using the set of parameters detailed in Fig. 9. This experimental procedure aimed to investigate the stochastic formation of humping in WA-DED parts and its progression to humping-induced porosity. As heat input decreased and travel speed increased, the deposited samples consistently exhibited flaw formation. However, an overlap of conditions was verified at a travel speed of 400 mm•min^{-1} and a heat input of 260 J•mm^{-1}, where both nominal and humping flawed parts were produced. Furthermore, reducing the heat input at high torch travel speeds intensified the humping flaw, promoting the formation of humping-induced porosity.

We note that there was no discernable difference in the current and voltage signals between humping, and humping-induced porosity.

In this work, we focused on understanding the causal relationship between the process state and meltpool dynamics. The rationale for introduction of variations in only travel speed used to produce the samples was motivated from the need to develop a robust model that would be able to detect process instability for different process parameters, irrespective of the processing parameters, instead of a model tailored for a fixed set of parameters.

For each of the 12 WA-DED samples produced, high-speed imaging was acquired for 2 layers. Hence, a total of 24 layers of data was acquired. Further, to avoid the transient behavior characteristic of the

initial layers in WA-DED, data acquisition commenced at layer 5. A second layer of data was sampled, when the buffer from the high-speed camera was completely cleared.

4. Observation and measurement of meltpool flow using high-speed imaging

4.1. Meltpool dynamics under nominal conditions

Fig. 10 shows the deposition of a layer under nominal conditions using images from the high-speed camera. In these images one complete short circuit cycle of material transfer is represented. There are four distinct phases in nominal deposition and in this illustration, each stage of material transfer mode is accompanied by an illustration of the phenomena.

In Fig. 10(a), the electric arc is stable and supplies heat to both the electrode and the meltpool. The molten droplet at the tip of the wire increases in size until material transfer occurs. The molten material on the surface of the meltpool is observed to be flowing toward the tail, in the direction opposite to that of the torch. This backflow on the surface is demarcated as x1, x2, and x3, which represents the distance from the edge of the electric arc to the brightest region of the surface of the meltpool. However, the height of the tail and front of the meltpool are relatively constant. This indicates that material at the bottom of the meltpool circulates from the tail toward the head. These internal flows agree with the process simulations reported by Cho et al. [19]. During this phase, the molten droplet at the tip of the wire is not visible due to the high intensity electromagnetic radiation emitted by the electric arc which surrounds the droplet. Next, the electric arc is extinguished as a short circuit occurs and material transfer is started as illustrated in Fig. 10(b). The transfer of material to the meltpool is completed in Fig. 10(c) when the molten droplet detaches from the wire. The electric arc is immediately reignited with the emission of spatter. Lastly, in Fig. 10(d) the electric arc stabilizes, resulting in a plasma column with constant size and volume.

4.2. Meltpool dynamics during humping

Fig. 11 illustrates the evolution of the meltpool during humping instability. For elucidation, we stratify the meltpool dynamics into four stages. In Fig. 11(a), a strong backflow is observed in the meltpool. Contrary to the nominal deposition condition in Fig. 10, where material depth in the tail and head was relatively similar, during humping the material continues to progressively accumulate at the tail. This is because the higher torch velocity disrupts the internal flow of material from the tail to the head of the meltpool.

The higher torch velocity (v) increases the momentum of material towards the meltpool tail and reduces the meltpool depth resulting in a shallower meltpool. This effect is evident in Fig. 11(a). Unlike the nominal conditions, where the height of the meltpool is similar at the front and tail regions, in the humping condition, the front of the meltpool is at a lower height than the molten material accumulating in the tail region.

As the torch continues to move, a shallow meltpool region or valley is formed, approximately halfway between the head and tail regions, as identified in Fig. 11(b). This shallow meltpool region is formed due to the elevated arc pressure and the momentum of the material in the direction of the meltpool tail.

Next, the low volume of molten material in the shallow valley region experiences rapid solidification. The solidified valley, illustrated in Fig. 11(c) prevents further flow of molten material between the tail and head of the meltpool. The meltpool is thus separated into two distinct regions at the head and tail of the meltpool. The relatively more volume of material aggregated in the tail region of the meltpool solidifies, albeit more slowly, resulting in a characteristic hump-like shape. The process continues with the formation of a smaller meltpool, Fig. 11(d), thus restarting the process of hump formation.

4.3. Meltpool dynamics during humping-induced porosity

Fig. 12 exemplifies the four stages of the genesis of humping-induced porosity flaw. As in humping, a strong backflow is observed in the meltpool, and relatively larger volume of molten material accumulates near the tail of the meltpool compared to the head as exemplified in Fig. 12(a). As explained in the context of Fig. 3, the severe variation in CTWD can lead to disruptions in the protective function of the shielding gas. The disruption of the shielding gas is liable to create porosity due to dissolution of atmospheric elements into the molten metal and

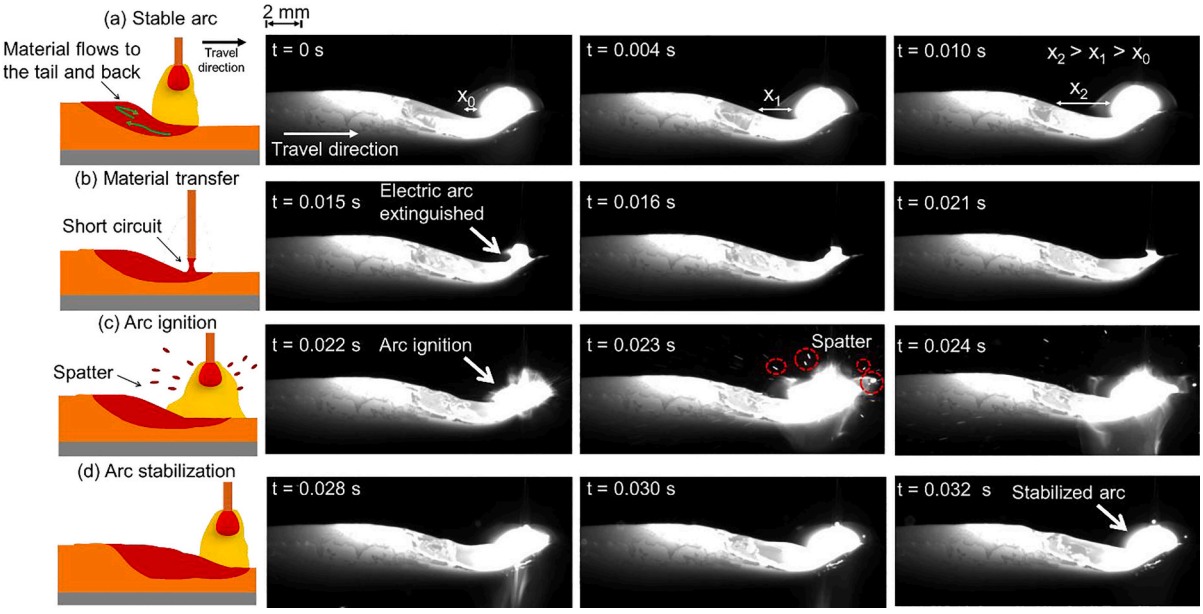

Fig. 10. Material transfer for a nominal WA-DED layer under short circuit transfer mode (supplementary video provided). (a) Electric arc supplies heat to the process (b) material transfer from the feedstock wire to the meltpool, inducing a short circuit condition. (c) Re-ignition of the electric arc restarts the deposition process, emitting spatter. (d) Electric arc re-stabilizes after ignition.

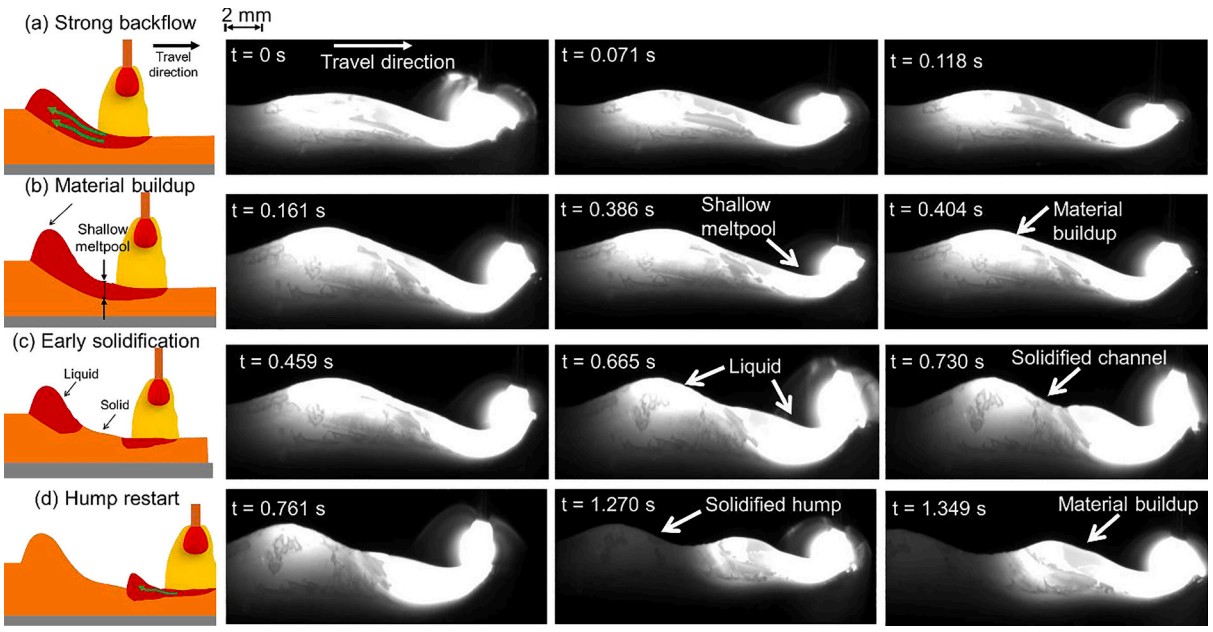

Fig. 11. Formation of a humping flaw (supplementary video provided). (a) Material begins building up at the tail of the meltpool due to the suppression of front flow inside the meltpool; (b) Movement of the torch leads to a shallow meltpool; (c) Liquid channel solidifies rapidly and separates the meltpool into two separate molten regions; and (d) the humping phenomena is restarted by the accumulation of material at the tail of the meltpool.

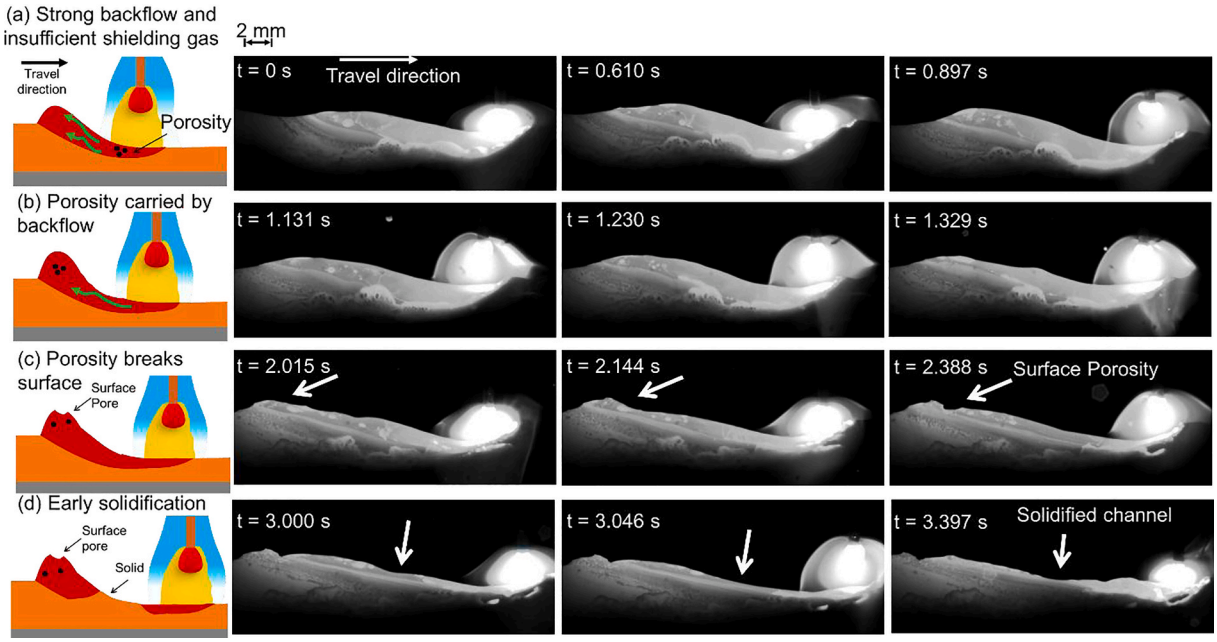

Fig. 12. Formation of a humping flaw (supplementary video provided). (a) the large variation in CTWD induces porosity in the meltpool, while the accumulation of material is being formed. (b) due to the lack of front flow the porosity is transported to the tail of the meltpool. (c) porosity breaks the surface tension of the meltpool. (d) early solidification divides the meltpool similarly to the observed for humping flaws.

introduction of contaminants from spatter into the meltpool [6].

As the meltpool develops and material is transferred, the strong backflow drags the internal porosity to the tail of the meltpool as illustrated in Fig. 12(b). Some pores in the tail may be conveyed to the surface of the meltpool, while other pores may be embedded deeper as observed in Fig. 12(c). Finally, as shown in Fig. 12(d), the valley region rapidly solidifies, restricting the flow of material to the tail. Since the tail of the meltpool is the last to solidify, the pores remain trapped within it. Finally, the process continues with the formation of a new meltpool with further pores.

4.4. Tracking of meltpool flow velocity

Continuing with the analysis, we measured and demarcated the difference in meltpool flow velocity for the three process conditions. In this research the meltpool flow velocity was estimated by tracking the motion of features on the surface of the meltpool, which are discernable in the high-speed images as they traverse from the meltpool head towards the meltpool tail.

Tracking the meltpool flow through the features on its surface is challenging given the dynamic nature of the process and high variability

in the electromagnetic radiation emitted by the electric arc. Consequently, to track the meltpool flow, a Sobel filter was applied to the raw high-speed images to enable accurate tracking of meltpool surface features [42]. The application of the Sobel filter to the raw image is illustrated in Fig. 13 – the filter parameters were determined through trial-and-error optimization. The X- and Z- coordinate locations of each meltpool surface features were identified in each frame of the high-speed images through visual observation.

The absolute meltpool flow velocity (v_f, [mm•s^{-1}]) is estimated by tracking the relative displacement ΔX and ΔZ of a surface feature across successive image frames, as $v_f = \sqrt{\left(\frac{\Delta Y}{\Delta t}\right)^2 + \left(\frac{\Delta Z}{\Delta t}\right)^2}$. Fig. 14 illustrates the identification and tracking of a meltpool feature for each process regime, represented across four frames. We note that for the nominal and humping-induced porosity conditions particle-like meltpool surface features were used to measure the flow, whist wave-like features were tracked for the humping condition. Due to the dynamic characteristics of the meltpool, these are observed to have varying shape and direction through the frames.

Five meltpool flow measurements were performed for each process regime; Fig. 15 illustrates the mean meltpool flow for nominal, humping, and humping-induced porosity along with the corresponding ± 1 standard deviation. The results indicate that the average meltpool flow velocity at the surface of the meltpool is higher during humping and humping-induced porosity conditions (200 to 300 mm•s^{-1}) compared to the nominal condition (125 mm•s^{-1}) due to the persistent backflow of the meltpool, as discussed in Sec. 4.2 and 4.3, and in close agreement with the literature [27]. Further, the meltpool flow velocity is significantly larger for humping-induced porosity (300 mm•s^{-1}) compared to humping (200 mm•s^{-1}) on account of the larger backflow. These results indicate that while humping and humping-induced porosity may appear similar, they involve distinct physical behaviors at the meltpool scale. A statistically significant difference (ANOVA, p-value of 0.003) was ascertained between the three process regimes. In the following section, we automate the detection of process instabilities using geometrical features extracted from the high-speed meltpool imaging data, through machine learning.

4.5. Process monitoring and machine learning

The meltpool images acquired from the high-speed camera are used for monitoring the process state. The aim is to classify the process state into nominal, humping, and humping-induced porosity. Specifically, physically-intuitive meltpool morphology features are extracted from the images. These meltpool morphology features are subsequently used as inputs to simple machine learning models, such as logistic regression, k-nearest neighbors, support vector machine, and shallow neural networks. These machine learning models are trained based on manually-labelled meltpool images.

The foregoing process monitoring approach is termed *process-aware machine learning* as it uses only four physically intuitive meltpool morphology features. As a benchmark, the results from the process-aware machine learning approach are compared with a deep learning, convolutional neural network algorithm that directly uses the meltpool images, as opposed to meltpool features. The process-aware machine learning approach comprises of three main steps: (i) image pre-processing, and (ii) feature extraction, and (iii) model training. These steps are described herewith.

4.6. Image pre-processing and feature extraction

Image pre-processing demarcates the meltpool boundary and separates it from surrounding artifacts, such as the wire, plume from the shielding gas, solidified layer, and reflections. The full pre-processing procedure was computationally implemented in the Python 3.7 programming language, with the support of the OpenCV library. A visual depiction of the pre-processing procedure is shown in Fig. 16 and is further detailed in Appendix A. Once the appropriate parameters for these steps are identified, they can operate on an image in an online manner.

The detection of the meltpool contour was achieved via three sequential computer vision procedures, namely: Gaussian blurring, two step binary thresholding, and border tracing [43]. The two initial procedures reduce the surrounding noise and detect the shape of the meltpool. The third procedure traces a closed border around the meltpool. First, a Gaussian blurring filter is applied to an input grayscale image of the meltpool region, as represented in Fig. 16(a) and (b). Gaussian blurring reduces the noise and smoothens the edges to improve the accuracy of the contour detection.

Second, the image is binarized using a fixed threshold, illustrated in Fig. 16(c), to differentiate between bright areas, which includes the meltpool region, and its surrounding noise. This fixed threshold was ascertained via heuristic observations, and remained fixed throughout. We note that in Fig. 16(d) the binarized image also includes the solidified layer and plume surrounding the meltpool. The binarized image is further analyzed pixel row-by-pixel row to eliminate artifacts, such as spatter particles. The largest contour or outer border from the pre-processed image largest contour is identified, as depicted with the red border in Fig. 16(d).

Third, after the identification of the outer contour, an adaptative threshold approach is employed to remove the solidified layer and plume, identified by the yellow shaded area in Fig. 16(e). Adaptative thresholding accounts for variations in pixel intensity caused by the variation of wire feed speed, and variations in background illumination and reflection of light from external objects. The resulting contour now only encompasses the desired meltpool boundary depicted in Fig. 16(e) and (f) with the green contour.

Finally, from the meltpool contour a so-called meltpool region skeleton is estimated encompassing the four fiducial coordinates shown in Fig. 16(f). These fiducials include the two farthest horizontal points in the travel direction, identified as the tail and front of the meltpool; the lowest point of the meltpool contour; and the centroid of the meltpool region. From these fiducials, four Euclidean distances and three angles

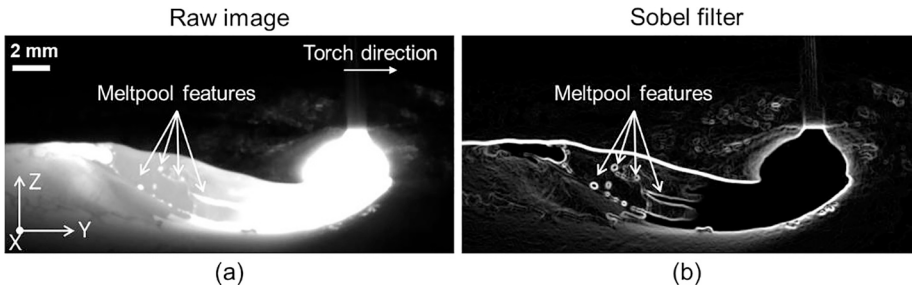

Fig. 13. Image processing and tracking of the meltpool features at the surface. (a) Raw image as acquired by the high-speed camera. (b) Application of the Sobel filter highlighting the edges of the constituents of the meltpool surface.

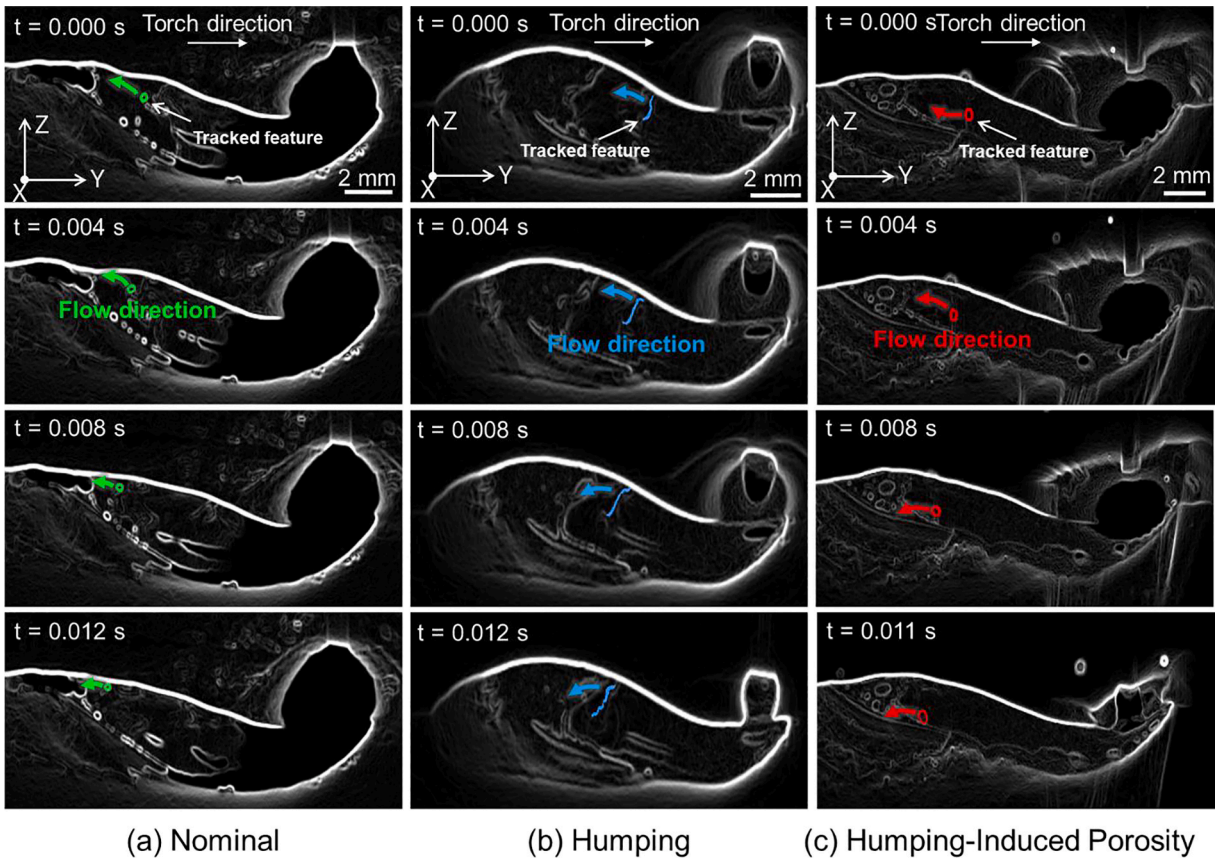

Fig. 14. Meltpool feature tracking for the process regimes identified in this study identifying the tracked feature and the direction of the flow. (a) Nominal process conditions. (b) Humping flaw formation. (c) Humping-induced porosity.

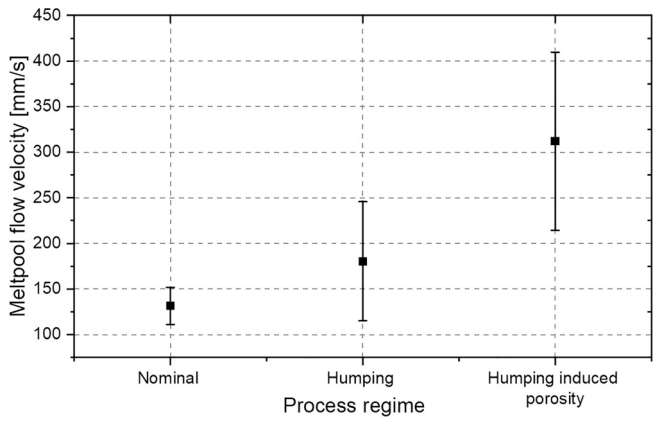

Fig. 15. Average and ±1 standard deviation meltpool flow velocity estimated from high-speed imaging for nominal, humping and humping-induced porosity. Humping and humping-induced porosity conditions reveal a higher meltpool flow velocity concordant with significant material backflow (n = 5 for each condition).

are identified. The rationale for these process signatures (features) is detailed in the following section.

Next, as shown in Fig. 17, a total of four meltpool shape or morphology features are extracted from the meltpool skeleton. These features (process signatures) are used as inputs for machine learning models. Each of the features extracted from the process images are detailed and their physical correlation to the process is explained.

The meltpool region area (A_m) is the number of pixels encompassed within the meltpool contour. The meltpool area is symptomatic of process instability. As previously illustrated in the context of humping (Fig. 11) and humping-induced porosity (Fig. 12), a sharp reduction in meltpool area is an indication of early solidification in the valley region of the meltpool on account of restricted material flow to the front of the meltpool.

Further, as depicted in Fig. 17, three angles, labeled α, β, and θ derived from the meltpool skeleton are used as features. The angles α and β are the angles subtended by the segment joining the tail and front fiducial points, and the centroid of the meltpool. Likewise, the angle θ is demarcated in Fig. 17. These angles estimate the curvature of the meltpool region on account of accumulation of material in the tail of the meltpool, characteristic of the humping and humping-induced porosity.

The rationale for selection of meltpool angles is further motivated in Fig. 18, in which a meltpool from the nominal layer is compared to a meltpool from a humping flawed layer. In Fig. 18(a), the angles, α0 and β0, for the nominal process state are larger than their counterparts α1 and β1, depicted in Fig. 18(b) during humping formation due to material buildup at the meltpool tail. This is because, the rapid solidification of the material in the valley region during humping, evident in Fig. 18(a), shifts the centroid further below. Likewise, Fig. 18(c) and (d) illustrates the changes in θ on account of humping formation. The accretion of material in the tail region of the meltpool, followed by rapid solidification of the layer takes a concave shape due to the humping geometry, resulting in a decrease of the θ angle.

Summarized in Fig. 19 is the statistical behavior of each of the four features with respect to the three process states. For example, the distribution of the meltpool area (A_m) in Fig. 19(a) whilst multi-modal, has distinctive differences between process states. The demarcation of process states is relatively more discernable from the distribution of the angles α, β and θ reported in Fig. 19(b)-(d). These qualitative results indicate that the onset of humping and humping-induced porosity,

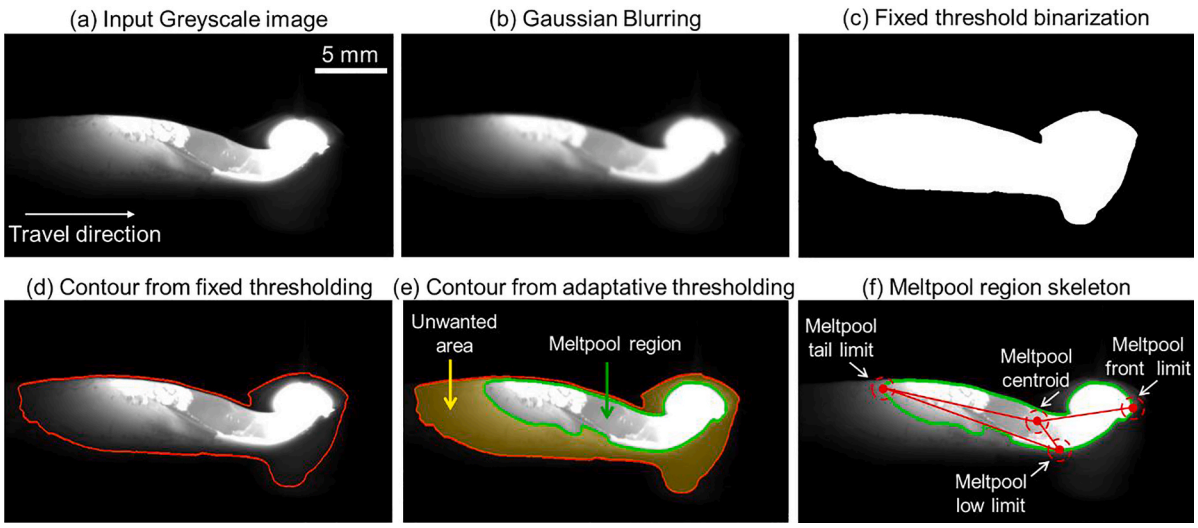

Fig. 16. Image pre-processing procedures: (a) input raw greyscale image. (b) gaussian blurring is applied to smooth the edges. (c) pixel binarization is applied by using a fixed threshold. (d) general contour detected from the fixed binarization. (e) adaptative binarization is used to identify the meltpool region and relegate the unwanted area from the final contour (green). (f) a meltpool "skeleton" is drawn, based on the computation of key angles and distances that link the melt pool contour extreme points and centroid. (For interpretation of the references to colour in this figure legend, the reader is referred to the web version of this article.)

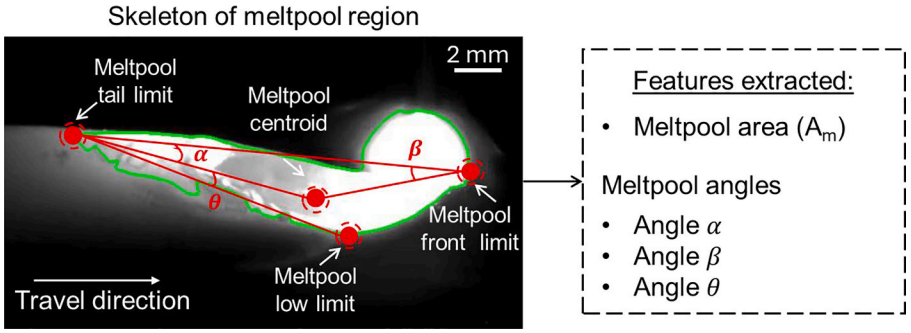

Fig. 17. Morphology features extracted from the skeleton: morphology is measured by the meltpool region area and by a set of angles that estimate the meltpool concavity and depth.

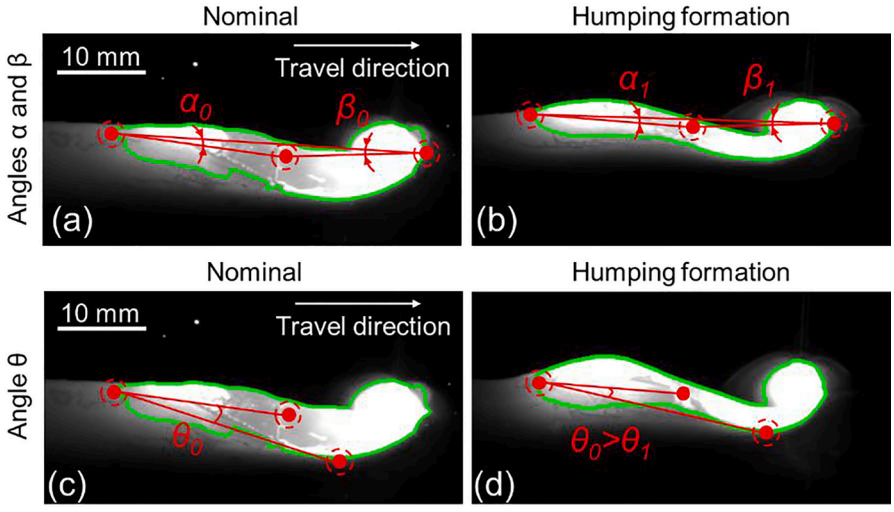

Fig. 18. Changes in angles α, β and θ for a deposition nominal and flawed conditions (material buildup at meltpool tail). (a) Angles α and β for a meltpool under nominal conditions. (b) No visible changes for both α and β when material accumulates at the tail of the meltpool. (c)Angle θ under nominal. (d) Angle θ decreases as material starts to build up at the meltpool tail indicating the start of the humping flaw.

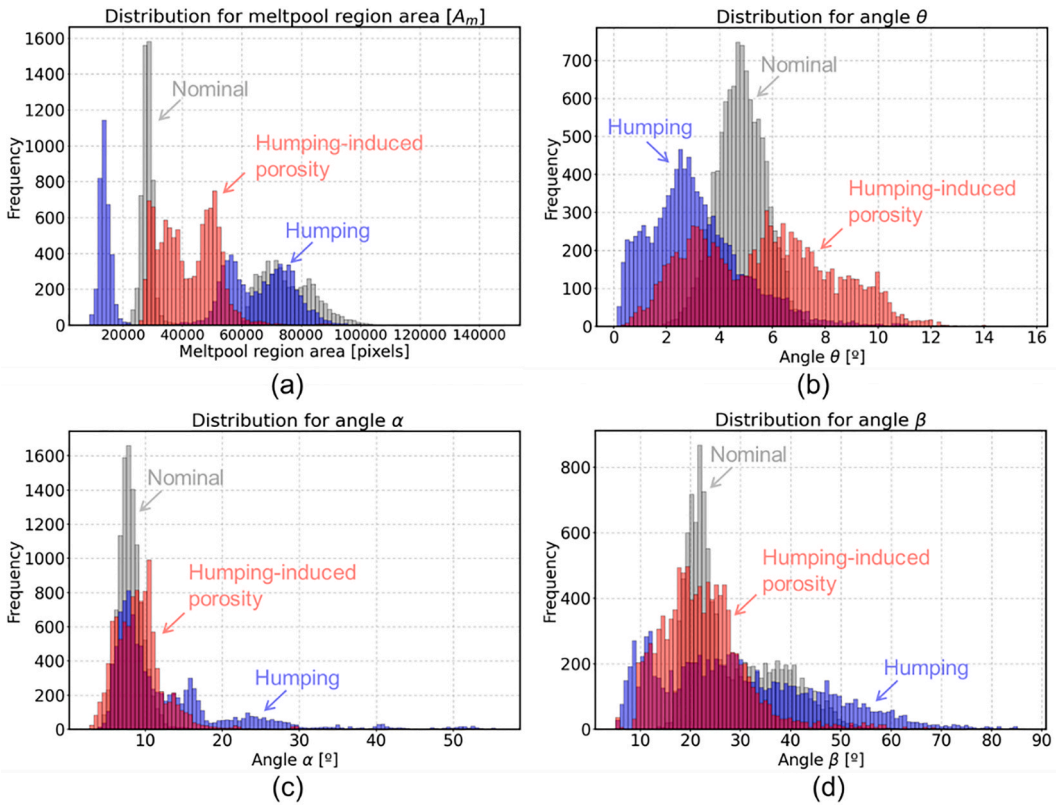

Fig. 19. Data distribution for the features extracted from the WA-DED process imaging: (a) Meltpool region area, (b) angle α, (c) angle θ, (d) angle β.

which affects the curvature of the meltpool, is reflected in the meltpool angles and area. However, given their complex statistical distributions there is a need to employ machine learning algorithms to discern trends within the data.

4.7. Machine learning

The general architecture of the process-aware machine learning approach is shown in Fig. 20. A hierarchical supervised machine learning approach was developed to classify the part condition based on the meltpool region morphology. The model architecture consists of two echelons. The first echelon classifies the process into either nominal state, i.e., flaw-free at a macro scale, or process instability encompassing both humping and humping-induced porosity conditions. The second echelon further stratifies the specific type of instability into humping or humping-induced porosity. The two-echelon approach minimized confounding between the two types of instabilities.

The need for a two-echelon machine learning model is rationalized as follows. In the initial stages of model development, a direct, single-class multi-class classification approach was tested. However, a single

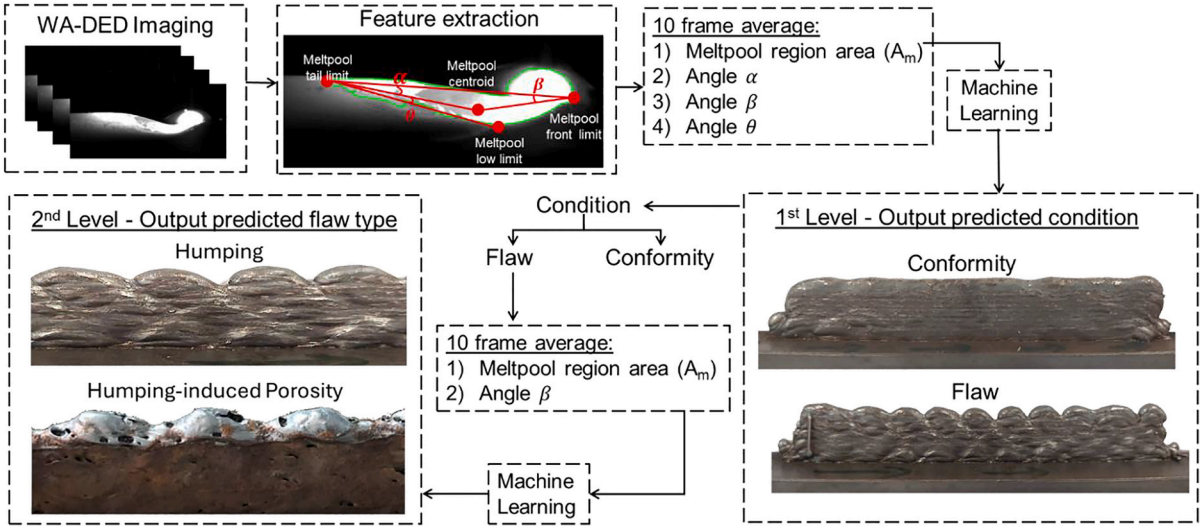

Fig. 20. Machine learning workflow: input meltpool images are pre-processed for contour detection and feature extraction of morphology and intensity data. Machine learning models are used to detect flaws (1st echelon) and the flawed layers are further classified into the specific type of flaw (2nd echelon) completing this two-hierarchy classification task.

echelon model failed to reliably distinguish (classify) between humping and humping-induced porosity with F1-score <50 %. This is likely due to, similarities between, and transient nature of humping and humping-induced porosity. As noted in the context of the high-speed imaging data in Sec. 4, humping and humping-induced porosity share several commonalities, and there is a large overlap in the meltpool features extracted (Fig. 19). To overcome the confusion between humping and humping-induced porosity, a two-echelon classification strategy was implemented where the first echelon just differentiates between a flawed and a flaw-free deposition, and the second echelon predicts the type of flaw.

To explain further, the first echelon classifying the process state as nominal or instability furnishes a relatively more balanced dataset concerning the type of instability in the second echelon. As represented in Fig. 20, a 10-frame moving average is applied to all the four input features to minimize the uncertainty resulting from variations in the tracing of the meltpool boundary.

Four extensively used supervised machine learning models were tested, based on their ease of implementation, namely: K-Nearest Neighbors (KNN), Logistic Regression (LR), Support Vector Machine (SVM), and a shallow Artificial Neural Network (ANN). At both echelons the same type of machine learning model is used. The classification fidelity for each of the models was measured in terms of the F1-score and the Mathews Correlation Coefficient (MCC). The F1-score assesses both false positive and false negative misclassifications while the MCC provides a robust metric for model performance with imbalanced datasets [44].

The relevant aspects of the implemented machine learning models are summarized in Table 2. These machine learning models were benchmarked against a pre-trained deep learning convolutional neural network (CNN) called Visual Graphics Group (VGG16) [45]. The VGG16 model is trained on the ImageNet dataset [46] (i.e., over 14 million labelled images) and its application to specific problems is operationalized via transfer learning. Due to its pre-trained nature and efficiency in image classification tasks this model is used in this research as the benchmark. This black box model was implemented in Python through the use of the TensorFlow library.

The training data was used to adjust the hyperparameters, summarized in Table 2. The model performance was assessed via 4-fold cross-validation on the training data. The training data subset is never aliased with testing data. The dataset for the first echelon was comprised of 30,996 total input–output pairs.

Further, a 64:36 training–testing data split was imposed. Considering these data divisions, a total of 20,351 datapoints were used for training while 10,645 datapoints were employed for testing of the model in the first echelon. The dataset is balanced such that there are 10,332 datasets for each of the three process states. The dataset was labeled on a layer-by-layer basis through visual observation. During the stratification of training and testing data, images from an entire individual layer were preferred over a randomized dataset to mitigate between layer variation from confounding the results.

Due to the transitory nature of humping and humping-induced porosity in the WA-DED process, and for purposes of balancing the acquired dataset, we used data acquired for 18 layers. For training, 12 layers were used, consisting of 4 layers representing the nominal condition, 4 humping, and 4 humping-induced porosity. Whilst 6 layers, distinct from the training layers, were quarantined for testing. The testing layers encapsulate: 2 nominal, 2 humping, and 2 humping-induced porosity layers.

All the layers labeled as unstable in the 1st echelon were also used to train and validate the 2nd echelon model. For the training and testing of this 2nd echelon, the dataset was comprised of 20,576 input–output pairs. The data is balanced; 10,049 datapoints belong to humping layers, and 10,521 data points to parts with humping-induced porosity layers. The training data for the second echelon comprises of 8 layers (4 layers for each type of instability), and 4 layers from each type were employed in the training and hyperparameter tuning of the models, while two layers from each were stored for model testing. The performance of the process-aware supervised machine learning models, i.e., KNN, LR, SVM, ANN were compared against a pre-trained deep learning CNN VGG16 architecture, which directly uses the raw, as-received meltpool images as inputs without the pre-processing and feature extraction steps previously discussed in this work.

Note on the need for segregating the meltpool images into layer-wise training and testing datasets: We deliberately used a layer-based stratification of the data for the composition of our training and validation datasets to avoid data leakage. In other words, the meltpool images for training and testing the model are sources from separate layers. Meltpool images for testing are not acquired from the same layer as the meltpool images used for model validation. This layer-wise data strategy is distinctive from the typically recommended randomized data split approach, where data is randomly assigned to training and validation classes. The randomized data split approach is not used herein because there is a high probability that the training and validation sets would have images with high spatio-temporal proximity and similarity, i.e. data leakage. This data leakage would cause the machine learning model to (misleadingly) have high predictability based on learn patterns specific to individual layers. Through the usage of entire layers exclusively used in training or in the validation of the models, we ensure that validation metrics are performed with inherently slightly different meltpool images, which in turn result in marginal changes in the features that were not previously seen by the model. We consider that the

Table 2
Relevant aspects of the four supervised machine learning models deployed in this work.

Model Type	Summary
Logistic Regression (LR)	– Linear discriminating equation – L2 regularization penalty – Inverse regularization strength (C): 0.00001 – Tolerance for stopping criterion: 0.001 – Solver: L-BFGS
Artificial Neural Network (ANN)	– Number of hidden layers: 2 – Number of neurons: 10 – Activation function: rectified linear unit – L2 Regularization – Solver: L-BFGS
Support Vector Machine (SVM)	– Soft margin classifier – Nonlinear kernel: Radial Basis – L2 Regularization – Kernel coefficient (gamma): 1 – Inverse regularization strength (C): 10 – Tolerance for stopping criterion: 0.001
K-Nearest Neighbors (KNN)	– Number of neighbors: 7 – Algorithm: Ball Tree – Distance metric: Manhattan

Table 3
Classification performance for all tested classification algorithms. Logistic Regression (LR); Artificial Neural Networks (ANN); Support Vector Machine (SVM); k-Nearest Neighbors (kNN); Visual Geometry Group 16 (VGG16).

Stage	Model	1st echelon (Flaw detection)		2nd echelon (Failure type detection)	
		F1-Score	MCC	F1-Score	MCC
Correlation (regression) model.	LR	80.6 %	0.000	65.8 %	0.012
Process-aware machine learning models.	**ANN**	**94.2 %**	**0.839**	**84.1 %**	**0.762**
	SVM	93.6 %	0.825	80.4 %	0.715
	kNN	93.0 %	0.812	57.0 %	0.5
Deep learning benchmark – Convolution neural network (CNN).	VGG16	74.1 %	0.601	66.8 %	0.138

layer-wise training and validation approach was essential to ensure an accurate description of the model's performance, and also ensure that the model would be generalizable.

The F1-score and MCC for each of the models for both echelons exclusively comprising of testing data with 10,332 meltpool images for each class, are summarized in Table 3 and visualized in Fig. 21. We reiterate that the first echelon focuses on flaw detection, i.e., nominal (conformity) vs. flaw formation; it does not distinguish between the type of flaw. The second echelon classifies the specific type of flaw.

All four process-aware machine learning models tested in this work have a classification accuracy (nominal vs unstable) exceeding 80 %, with the ANN achieving F1-Scores ≈ 94 %. Apart from the F1-score we also computed the MCC, viz., a performance metric for binary classifications, especially if the dataset was unbalanced. The MCC ranges between 1 and −1; 1 for a perfect prediction, –1 for an inverse prediction; and 0 for a random guess. The MCC considers all the elements in the confusion matrix, making it suitable for evaluating unbalanced datasets, contrary to the F1-score which does not consider the true negative elements. Albeit the dataset in this work was balanced, we chose to report the MCC in addition to the F1-scores for all the models tested to provide a single metric that accounts for all the predicted elements in the confusion matrix.

While most of the models show an MCC above 0.8 for the first echelon, the simple logistic regression (LR) model has an MCC of 0, equivalent to a random prediction of process state, indicating that simple correlation-based linear models are incapable of detecting incipient process flaws. The failure in identifying the process states originates from the major overlap in the data distribution of the features for each process states considered, in addition to the complex relation between those features, which cannot be identified by simple linear correlations.

In the second echelon, where the model distinguishes between the type of flaw, i.e., humping and humping-induced porosity, a decrease in model performance is noticeable throughout all models tested when compared to the first echelon. This performance deterioration in the second echelon underscores the complexity of providing an accurate distinction between humping and humping-induced flaws. Despite the generalized reduction in model performance, the process-aware ANN model reported the F1-score of 84.1 % and an MCC of 0.762. By contrast, the VGG16 as a benchmark representative of black-box deep-learning model, achieved F1-score of 74 % and 66 % for the first and second echelon, respectively, with a corresponding MCC of 0.601 and 0.138. These classification results highlight the utility of high-speed meltpool imaging to detect process flaws in WA-DED. Additionally, these results show that the process-aware models outperform the VGG16 black-box deep learning model in both echelons, i.e., detection and classification of instabilities.

Note on model generalizability: While the model predicted the onset of process instability with F1-score approaching 85 %, these results are specific to ER90S-G mild steel. The transferability of the model to other materials, such as aluminum, titanium alloys, Inconel is likely to be limited, because the material properties, such as thermal conductivity, viscosity, or melting point have a consequential effect on the meltpool dynamics [47]. Therefore, while the extracted meltpool features are likely to capture process instability, the model would likely require retraining due to a change in the interaction between the features. Additionally, variation in the welding process also have an effect on the meltpool dynamics [48]. Lastly, the current machine learning pipeline is based on extraction of simple, process-aware feature from high-speed imaging of the meltpool region to enable future real-time monitoring and closed—loop process control.

5. Conclusions and future work

In this work we elucidated through in-operando high-speed imaging the causal meltpool-scale phenomena at the root of humping and humping porosity process instabilities in WA-DED. Further, the high-speed imaging data was used for real-time monitoring of process instabilities.

Through analysis of the meltpool imaging we identified the dynamic meltpool phenomena inherent to humping and humping-porosity instabilities formation. The observed formation of the humping flaw was consistent with the numerical simulations in the literature. These observations explain the genesis of sub-surface and surface-level porosity in WA-DED. To summarize, in humping, material accretion in the tail region of the meltpool combined with the restricted flow of material toward the front of the meltpool causes a deep valley that rapidly solidifies relative to the rest of the meltpool. Humping-induced porosity occurs as a result of severe, unchecked humping instability which cause variations in the contact tip-to-work distance (CTWD), disrupting the flow of the shielding gas.

Next, we extracted four meltpool-related features (process signatures) symptomatic of process state from the high-speed meltpool images, and subsequently, employed these features as inputs to machine learning models. This *process-aware machine learning* approach requires just four meltpool morphology features, and provide detection fidelity ≈ 84 % (F1-score). By comparison, a complex, deep learning model that directly uses the data without leveraging any insight into the causal physics, is capable of F1-score < 66 %.

The main limitation of this work is that the high-speed imaging camera is in a staring configuration (Eulerian reference frame). Hence, the approach is constrained to single-bead, thin-wall parts. The sensing setup also does not account for the production of overhang geometries where the meltpool shape may change. To overcome this limitation, in

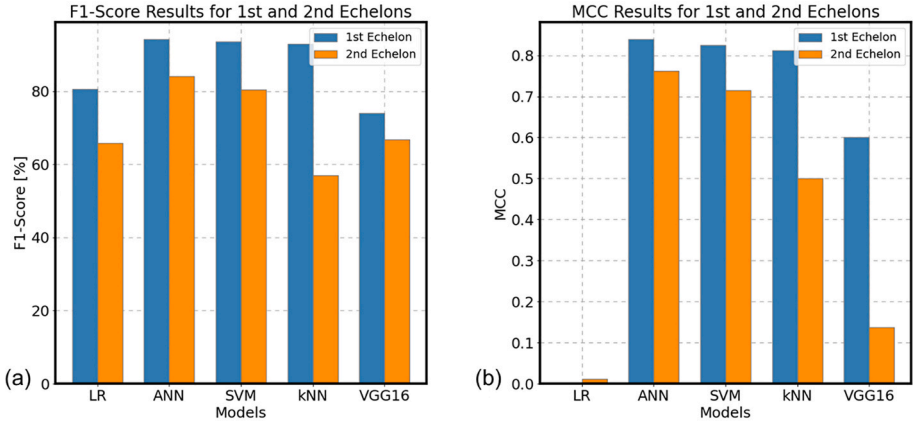

Fig. 21. Bar plot of the model results for 1st and 2nd echelon. (a) F1-Score (b) Mathew's Correlation Coefficients.

our future work, we will install the camera such that it translates along with the torch (Lagrangian reference frame), thus enabling monitoring of multi-bead parts with complex geometries. Furthermore, we will endeavor to identify and detect additional flaws such as cracking and lack-of-fusion porosity using a similar approach.

CRediT authorship contribution statement

André Ramalho: Writing – original draft, Methodology, Investigation. **Anis Assad:** Writing – original draft, Investigation, Formal analysis. **Benjamin Bevans:** Investigation, Formal analysis. **Fernando Deschamps:** Supervision. **Telmo G. Santos:** Writing – review & editing, Supervision. **J.P. Oliveira:** Writing – review & editing, Supervision, Project administration, Investigation. **Prahalada Rao:** Writing – review & editing, Supervision, Project administration, Formal analysis.

Declaration of competing interest

The authors declare that they have no known competing financial interests or personal relationships that could have appeared to influence the work reported in this paper.

Acknowledgements

AR, TGS and JPO acknowledge the Portuguese Fundação para a Ciência e a Tecnologia (FCT - MCTES) for its financial support via the project UIDB/00667/2020 and UIDP/00667/2020 (UNIDEMI). JPO acknowledges the funding by national funds from FCT - Fundação para a Ciência e a Tecnologia, I.P., in the scope of the projects LA/P/0037/2020, UIDP/50025/2020 and UIDB/50025/2020 of the Associate Laboratory Institute of Nanostructures, Nanomodelling and Nanofabrication – i3N. AR acknowledges FCT - MCTES for funding the PhD grant UI/BD/151018/2021. This activity has received funding from the European Institute of Innovation and Technology (EIT) RawMaterials through the project Smart WAAM: Microstructural Engineering and Integrated Non-Destructive Testing. This body of the European Union receives support from the European Union's Horizon 2020 research and innovation program.

Prahalada Rao gratefully acknowledges funding from the following US federal government agencies for nurturing his scholastic research in metal additive manufacturing and smart manufacturing over the last decade through the following awards. National Science Foundation (NSF) via Grant Nos. CMMI-2428305, CMMI-2336449, CMMI-2309483/1752069, OIA-1929172, PFI-TT 2322322/2044710, CMMI-1920245, ECCS-2020246, CMMI-1739696, CMMI-2336449, and CMMI-2428305; US Department of Navy, Naval Surface Warfare Center (NAVAIR, N6833524C0215) and Office of Naval Research (ONR, N00014-21-1-2781); and the National Institute of Standards and Technology (NIST, 70NANB23H029T). Understanding the causal influence of process parameters on part quality and detection of defect formation using in-situ sensing was the major aspect of CMMI-2309483/1752069 (Program Officer: Pranav Soman). The use of machine learning and analytics for process diagnosis in additive manufacturing was funded via ECCS-2020246 (program officer: Richard Nash). Benjamin Bevans was funded through CMMI-2309483/1752069 and PFI-TT 2322322/2044710.

Anis Assad and Fernando Deschamps were funded by the Coordenação de Aperfeiçoamento de Pessoal de Nível Superior – Brasil (CAPES) – Finance Code 001. The foregoing also funded a visiting student scholarship for Anis Assad to work at Virginia Tech under the supervision of Prahalada Rao.

Appendix A:. Image pre-processing algorithm.

Algorithm 1 – Image pre-processing: A computer vision approach is applied to detect the contour of the meltpool and to draw the meltpool skeleton.

Input: grayscale meltpool image
Apply gaussian blur
Binarize meltpool image with an initial threshold $T = 30$ pixels
For every image row **do**:
Count non-zero pixels for the row
If count ≤ 20 **then**:
Nullify full row
Detect biggest contour in the meltpool image
Compute the average grayscale intensity μ within the contour
Update the binary threshold $T = \mu \bullet 1.1$
If $T \leq$ maximum pixel value within the contour **then**:
Binarize meltpool image with threshold T
Else:
Binarize meltpool image with threshold μ
Detect biggest contour in the binarized image
Detect the meltpool left limit, right limit, low limit, and centroid from the biggest contour

Data availability

Data will be made available on request.

References

[1] D.-G. Ahn, Directed energy deposition (DED) process: state of the art, Int. J. Precis. Eng. Manuf.-Green Technol. 8 (2021) 703–742, https://doi.org/10.1007/s40684-020-00302-7.
[2] T.A. Rodrigues, V. Duarte, R.M. Miranda, T.G. Santos, J.P. Oliveira, Current status and perspectives on wire and arc additive manufacturing (WAAM), Materials 12 (2019) 1121, https://doi.org/10.3390/ma12071121.
[3] W. Jin, C. Zhang, S. Jin, Y. Tian, D. Wellmann, W. Liu, Wire arc additive manufacturing of stainless steels: a review, Appl. Sci. 10 (2020) 1563, https://doi.org/10.3390/app10051563.
[4] S.R. Singh, P. Khanna, Wire arc additive manufacturing (WAAM): a new process to shape engineering materials, Mater. Today Proc. 44 (2021) 118–128, https://doi.org/10.1016/j.matpr.2020.08.030.
[5] B. Mvola, P. Kah, Effects of shielding gas control: welded joint properties in GMAW process optimization, Int. J. Adv. Manuf. Technol. 88 (2017) 2369–2387, https://doi.org/10.1007/s00170-016-8936-2.
[6] S. Srivastava, R.K. Garg, Process parameter optimization of gas metal arc welding on IS:2062 mild steel using response surface methodology, J. Manuf. Process. 25 (2017) 296–305, https://doi.org/10.1016/j.jmapro.2016.12.016.
[7] B. Saleh, R. Fathi, Y. Tian, N. Radhika, J. Jiang, A. Ma, Fundamentals and advances of wire arc additive manufacturing: materials, process parameters, potential applications, and future trends, Arch. Civ. Mech. Eng. 23 (2023) 96, https://doi.org/10.1007/s43452-023-00633-7.
[8] T. Ron, O. Dolev, A. Leon, A. Shirizly, E. Aghion, Effect of phase transformation on stress corrosion behavior of additively manufactured austenitic stainless steel

produced by directed energy deposition, Materials 14 (2020) 55, https://doi.org/10.3390/ma14010055.
[9] B.T. Gibson, Y.K. Bandari, B.S. Richardson, W.C. Henry, E.J. Vetland, T. W. Sundermann, L.J. Love, Melt pool size control through multiple closed-loop modalities in laser-wire directed energy deposition of Ti-6Al-4V, Addit. Manuf. 32 (2020) 100993, https://doi.org/10.1016/j.addma.2019.100993.
[10] H. Siva Prasad, F. Brueckner, A.F.H. Kaplan, Powder incorporation and spatter formation in high deposition rate blown powder directed energy deposition, Addit. Manuf. 35 (2020) 101413, https://doi.org/10.1016/j.addma.2020.101413.
[11] A. Nycz, M.W. Noakes, B. Richardson, A. Messing, B. Post, J. Paul, J. Flamm, L. Love, Challenges in making complex metal large-scale parts for additive manufacturing: a case study based on the additive manufacturing excavator, in: Solid Freeform Fabrication 2017: Proceedings of the 28th Annual International Solid Freeform Fabrication Symposium – An Additive Manufacturing Conference, Austin, TX, USA, 2017.
[12] Y.G.Y. Elshaghoul, M.M. El-Sayed Seleman, A. Bakkar, S.A. Elnekhaily, I. Albaijan, M.M.Z. Ahmed, A. Abdel-Samad, R. Reda, Additive friction stir deposition of AA7075-T6 alloy: impact of process parameters on the microstructures and properties of the continuously deposited multilayered parts, Appl. Sci. 13 (2023) 10255, https://doi.org/10.3390/app131810255.
[13] F. Li, S. Chen, J. Shi, H. Tian, Y. Zhao, Evaluation and optimization of a hybrid manufacturing process combining wire arc additive manufacturing with milling for the fabrication of stiffened panels, Appl. Sci. 7 (2017) 1233, https://doi.org/10.3390/app7121233.
[14] N. Grossi, A. Scippa, G. Venturini, G. Campatelli, Process parameters optimization of thin-wall machining for wire arc additive manufactured parts, Appl. Sci. 10 (2020) 7575, https://doi.org/10.3390/app10217575.
[15] A.I. Albannai, A brief review on the common defects in wire arc additive manufacturing, Int. J. Current Sci. Res. Rev. 05 (2022), https://doi.org/10.47191/ijcsrr/V5-i12-19.
[16] S. Tammas-Williams, P.J. Withers, I. Todd, P.B. Prangnell, The influence of porosity on fatigue crack initiation in additively manufactured titanium components, Sci. Rep. 7 (2017) 7308, https://doi.org/10.1038/s41598-017-06504-5.
[17] E. Akgun, X. Zhang, R. Biswal, Y. Zhang, M. Doré, Fatigue of wire+arc additive manufactured Ti-6Al-4V in presence of process-induced porosity defects, Int. J. Fatigue 150 (2021) 106315, https://doi.org/10.1016/j.ijfatigue.2021.106315.
[18] E. Soderstrom, P. Mendez, Humping mechanisms present in high speed welding, Sci. Technol. Weld. Join. 11 (2006) 572–579, https://doi.org/10.1179/174329306X120787.
[19] Y. Ai, P. Jiang, C. Wang, G. Mi, S. Geng, W. Liu, C. Han, Investigation of the humping formation in the high power and high speed laser welding, Opt. Lasers Eng. 107 (2018) 102–111, https://doi.org/10.1016/j.optlaseng.2018.03.010.
[20] X. Meng, G. Qin, Z. Zou, Characterization of molten pool behavior and humping formation tendency in high-speed gas tungsten arc welding, Int. J. Heat Mass Transf. 117 (2018) 508–516, https://doi.org/10.1016/j.ijheatmasstransfer.2017.09.124.
[21] B. Bevans, A. Ramalho, Z. Smoqi, A. Gaikwad, T.G. Santos, P. Rao, J.P. Oliveira, Monitoring and flaw detection during wire-based directed energy deposition using in-situ acoustic sensing and wavelet graph signal analysis, Mater. Des. 225 (2023) 111480, https://doi.org/10.1016/j.matdes.2022.111480.
[22] E. Wei, D. Farson, R. Richardson, H. Ludewig, Detection of weld surface porosity by statistical analysis of arc current in gas metal arc welding, J. Manuf. Process. 3 (2001) 50–59, https://doi.org/10.1016/S1526-6125(01)70033-3.
[23] I. Bitharas, N.A. McPherson, W. McGhie, D. Roy, A.J. Moore, Visualisation and optimisation of shielding gas coverage during gas metal arc welding, J. Mater. Process. Technol. 255 (2018) 451–462, https://doi.org/10.1016/j.jmatprotec.2017.11.048.
[24] C.S. Wu, L.M. Zhong, J.Q. Gao, Visualization of hump formation in high-speed gas metal arc welding, Meas. Sci. Technol. 20 (2009) 115702, https://doi.org/10.1088/0957-0233/20/11/115702.
[25] J. Chen, C.-S. Wu, Numerical analysis of forming mechanism of hump bead in high speed GMAW, Weld. World 54 (2010) 286–291, https://doi.org/10.1007/BF03266741.
[26] T.C. Nguyen, D.C. Weckman, D.A. Johnson, H.W. Kerr, The humping phenomenon during high speed gas metal arc welding, Sci. Technol. Weld. Join. 10 (2005) 447–459, https://doi.org/10.1179/174329305X44134.
[27] M.H. Cho, D.F. Farson, Understanding bead hump formation in gas metal arc welding using a numerical simulation, Metall. Mater. Trans. B 38 (2007) 305–319, https://doi.org/10.1007/s11663-007-9034-5.
[28] D. Wu, X. Hua, D. Ye, F. Li, Understanding of humping formation and suppression mechanisms using the numerical simulation, Int. J. Heat Mass Transf. 104 (2017) 634–643, https://doi.org/10.1016/j.ijheatmasstransfer.2016.08.110.
[29] Y. Gu, X. Hua, D. Ye, F. Li, X. Ma, C. Xu, Numerical simulation of hump suppression in high-speed triple-wire GMAW, Int. J. Adv. Manuf. Technol. 89 (2017) 727–734, https://doi.org/10.1007/s00170-016-9119-x.
[30] A. Adebayo, J. Mehnen, X. Tonnellier, Limiting Travel Speed in Additive Layer Manufacturing, in: 9th International Conference on Trends in Welding Research, ASM International, Chicago, IL, USA, 2012.
[31] K. Sawrav, P.P. Bandyopadhyay, Relationship of dew point and ambient temperature variation on weld quality, Int. J. Ind. Eng.Theory Appl. Pract. 30 (2023) 491–505, https://doi.org/10.23055/ijietap.2023.30.2.8799.
[32] V. Beyer, S.W. Campbell, G.M. Ramsey, A.M. Galloway, A.J. Moore, N. A. McPherson, Systematic study of effect of cross-drafts and nozzle diameter on shield gas coverage in MIG welding, Sci. Technol. Weld. Join. 18 (2013) 652–660, https://doi.org/10.1179/1362171813Y.0000000143.
[33] W. Li, H. Zhang, G. Wang, G. Xiong, M. Zhao, G. Li, R. Li, Deep learning based online metallic surface defect detection method for wire and arc additive manufacturing, Robot. Comput. Integr. Manuf. 80 (2023) 102470, https://doi.org/10.1016/j.rcim.2022.102470.
[34] C. Xia, Z. Pan, Y. Li, J. Chen, H. Li, Vision-based melt pool monitoring for wire-arc additive manufacturing using deep learning method, Int. J. Adv. Manuf. Technol. 120 (2022) 551–562, https://doi.org/10.1007/s00170-022-08811-2.
[35] T. Hauser, A. Da Silva, R.T. Reisch, J. Volpp, T. Kamps, A.F.H. Kaplan, Fluctuation effects in Wire Arc Additive Manufacturing of aluminium analysed by high-speed imaging, J. Manuf. Process. 56 (2020) 1088–1098, https://doi.org/10.1016/j.jmapro.2020.05.030.
[36] Q. Zhan, Y. Liang, J. Ding, S. Williams, A wire deflection detection method based on image processing in wire + arc additive manufacturing, Int. J. Adv. Manuf. Technol. 89 (2017) 755–763, https://doi.org/10.1007/s00170-016-9106-2.
[37] U. Reisgen, S. Mann, L. Oster, P. Lozano, R. Sharma, Study on workpiece and welding torch height control for polydirectional WAAM by means of image processing, in: In: 2019 IEEE 15th International Conference on Automation Science and Engineering (CASE), 2019, pp. 6–11, https://doi.org/10.1109/COASE.2019.8843076.
[38] J. Franke, F. Heinrich, R.T. Reisch, Vision based process monitoring in wire arc additive manufacturing (WAAM), J. Intell. Manuf. 36 (2025) 1711–1721, https://doi.org/10.1007/s10845-023-02287-x.
[39] J. Xiong, Y. Zhang, Y. Pi, Control of deposition height in WAAM using visual inspection of previous and current layers, J. Intell. Manuf. 32 (2021) 2209–2217, https://doi.org/10.1007/s10845-020-01634-6.
[40] J. Xiong, M. Shi, Y. Liu, Z. Yin, Virtual binocular vision sensing and control of molten pool width for gas metal arc additive manufactured thin-walled components, Addit. Manuf. 33 (2020) 101121, https://doi.org/10.1016/j.addma.2020.101121.
[41] A. Joseph, D. Farson, D. Harwig, R. Richardson, Influence of GMAW-P current waveforms on heat input and weld bead shape, Sci. Technol. Weld. Join. 10 (2005) 311–318, https://doi.org/10.1179/174329305X40624.
[42] N. Kanopoulos, N. Vasanthavada, R.L. Baker, Design of an image edge detection filter using the Sobel operator, IEEE J. Solid-State Circuits 23 (1988) 358–367, https://doi.org/10.1109/4.996.
[43] J.M. Blackledge, Segmentation and Edge Detection, in: Digital Image Processing: Mathematical and Computational Methods, 1st Edition, Horwood Publishing Limited, West Sussex, England, 2005: pp. 487–511. doi:10.1533/9780857099464.4.486.
[44] D. Chicco, G. Jurman, The advantages of the Matthews correlation coefficient (MCC) over F1 score and accuracy in binary classification evaluation, BMC Genomics 21 (2020) 6, https://doi.org/10.1186/s12864-019-6413-7.
[45] K. Simonyan, A. Zisserman, Very deep convolutional networks for large-scale image recognition, in: In: International Conference on Learning Representations (ICLR 2015), 2015, https://doi.org/10.48550/arXiv.1409.1556.
[46] J. Deng, W. Dong, R. Socher, L.-J. Li, Kai Li, Li Fei-Fei, ImageNet: a large-scale hierarchical image database, in: In: 2009 IEEE Conference on Computer Vision and Pattern Recognition, 2009, pp. 248–255, https://doi.org/10.1109/CVPR.2009.5206848.
[47] D. Galeazzi, R.H.G. e Silva, A.B. Viviani, P.R. Jaeger, M.B. Schwedersky, Evaluation of thermal and geometric properties of martensitic stainless steel thin walls built by additive manufacturing cold metal transfer (CMT) processes, Int. J. Adv. Manuf. Technol. 120 (2022) 2151–2165, https://doi.org/10.1007/s00170-022-08921-x.
[48] H. Stinson, R. Ward, J. Quinn, C. McGarrigle, Comparison of properties and bead geometry in MIG and CMT single layer samples for WAAM applications, Metals (basel) 11 (2021) 1530, https://doi.org/10.3390/met11101530.